J Mater Sci: Mater Electron (2023) 34:387

Dielectric behavior and phase transition of $La_2Mo_2O_9$ films synthesized by spray pyrolysis technique

Govinda A. Kadam[1], Sagar A. Patil[2], Bajarang B. Patil[3], Sarita S. Kumbhar[4], Sambhaji S. Kumbhar[2], Suraj B. Madake[4], Laxman D. Kadam[4], Yuan-Ron Ma[5], Sujit A. Kadam[5,*], and Rajesh K. Nimat[1,*]

[1] *Department of Physics, Balasaheb Desai College, Patan, Maharashtra 415206, India*
[2] *Centre for Interdisciplinary Research, D. Y. Patil Education Society, Kasaba Bawada, Kolhapur, Maharashtra 416006, India*
[3] *PG Department of Physics, Balwant College, Vita, Maharashtra 415311, India*
[4] *Department of Physics, Shivaji University, Kolhapur, Maharashtra 416004, India*
[5] *Department of Physics, National Dong Hwa University, Hualien 97401, Taiwan*

Received: 11 November 2022
Accepted: 27 December 2022
Published online: 4 February 2023

ABSTRACT

The novel fast oxide ion-conducting material $La_2Mo_2O_9$ (LAMOX) thin films were synthesized by using the cost-effective chemical spray pyrolysis technique. Thermal Gravimetric and differential thermal analysis show the phase transition of $La_2Mo_2O_9$ from α-monoclinic to β-cubic phase at 546.5 °C. Rietveld refinement confirms the stabilization of the β-cubic phase for $La_2Mo_2O_9$ thin films at high temperature. The porous morphology was observed after the annealing and the XPS study revealed elements La, Mo and O observed on the surface of thin films. The temperature and frequency-dependent dielectric constant were studied using an LCR-Q meter in the frequency range of 20 Hz–300 kHz. As the frequency increases, the dielectric constant and dielectric loss decreases for all $La_2Mo_2O_9$ thin films. The dielectric constant, dielectric loss and AC conductivity varied with increasing temperature, shows two relaxation peaks indicating the presence of oxide ion vacancies for ion conduction. The complex impedance shows the Cole–Cole plot for the LAMOX thin films.

1 Introduction

A fuel cell is an electrochemical device that converts chemical energy directly into electrical energy with the water as a by-product [1, 2]. The oxide ion-conducting materials are the interesting materials because of its application mainly in fields like oxygen sensors, oxygen pumps, oxygen separation membranes and solid oxide fuel cells [3–8]. In 2000, Lacorre [5] discovered the new fast oxide ion-conducting material and illustrated that the lanthanum molybdenum oxide ($La_2Mo_2O_9$) possesses greater ion conduction ability at 800 °C than the conventional oxide ion conductor Yttria Stabilized Zirconia (YSZ). The phase transition of $La_2Mo_2O_9$ takes place from low oxide ion conducting α-monoclinic to high oxide

Address correspondence to E-mail: ksujit17@gmail.com; rajeshknimat@gmail.com

https://doi.org/10.1007/s10854-022-09796-0

ion conducting β-cubic at around 580 °C, the ionic conductivity of $La_2Mo_2O_9$ increases its order twice after phase transition [9–12]. It has been found that the crystallographic sites of β-$La_2Mo_2O_9$ for the occupation of oxygen ions are partially available, which increases the concentration of oxide ion vacancy, which delivers sufficient paths for the diffusion of oxygen ions, and subsequently, the oxide ionic conduction is high for β-cubic $La_2Mo_2O_9$ [13, 14]. The drastic change observed in ion conduction and lattice parameter of $La_2Mo_2O_9$ due to the phase transition from low α-monoclinic to β-cubic phase [15, 16]. Many recent studies have been carried out to lower the phase transition temperature and maintain the high oxide ion conductivity for $La_2Mo_2O_9$ β-cubic phase [17]. $La.^{3+}$ based compounds also shows optical, dielectric and magnetic properties [18, 19]

Nowadays, researchers in the field of material science, physics, technology and chemistry have reported novel applications in various fields like electrochemical hydrogen storage [20, 21] photocatalytic activity [22–24], antimicrobial characteristics [25–27] etc. The properties of $La_2Mo_2O_9$ make it more beneficiary metal oxides than other metals like $DyBa_2Fe_3O_{7.988}/DyFeO_3$ [27] $Dy_2BaCuO_5/Ba_4DyCu_3O_{9.09}$ [26], Co/Co_3O_4 [25], $BaDy_2NiO_5/NiO$ [24], $Zn_{0.35}Fe_{2.65}O_4$ [23], $DyMn_2O_5/Ba_3Mn_2O_8$ [20], $CdHgI_4/HgI_2$ [28], Ni/NiO [22], Fe_2O_3 [29] in various applications. The increasing microelectronics industrial necessitates and shrinking of device components ranging from transistors to energy storage devices makes the materials is more efficient for high-performance applications. On other hand, the shrinking of integrated circuits has resulted in excessive power consumption and signal delays in their interconnections [30, 31]. To address these constraints, insulating materials with low dielectric constants have been investigated [32–35]. Additionally, these low dielectric loss materials have significant prospective applications in domains of interlayer dielectrics, semiconductor packaging (chips, modules), high frequency devices, low-loss boards [36] etc.

Researchers mostly studied lanthanum oxide compounds for various synthetic techniques for the evaluation of dielectric properties. Suzuki et al. [37] used the Metal Oxide Chemical Vepor Deposition process to create La-oxide and La-oxide/SiON films on Si substrates. Furthermore, Krishna et al. [38] created lanthanum oxide nanoparticles for dielectric characteristics utilizing a chemical co-precipitation technique. In contrast, the lanthanum oxide doped lithium borosilicate glasses were made by Ganviraet et al. [39]. Using a typical melt-quenching process for electrical and dielectric property studies, Gopalakrishnan et al. [40] investigated the dielectric properties of $LaMoO_x$ and synthesized the $La_4Mo_7O_{27}$ by adopting high-temperature solution growth technique.

Goutenoire et al. [6] reported that the β-cubic phase $La_2Mo_2O_9$ is more disordered structure, which contains three oxygen sites O_1 at 4a site are fully occupied whereas O_2 and O_3 at 12b partially occupied Wyckoff positions is the key part of the β-cubic phase of $La_2Mo_2O_9$. Fournier et al. [41] successful synthesis the $La_2Mo_2O_9$ using conventional solid-state techniques. The material under investigation owing to its outstanding properties, it has also prepared using mechanochemical synthesis [42], sol–gel routes [43] and freeze-dried precursors [44]. These synthesis methods are more time consuming it takes times from several hours to even in days to complete phase formation as compared to spray pyrolysis method. The spray pyrolysis method is time efficient and take less time, low-cost and suitable for the formation of nanoscale particals.

The present study investigate the pores structure pristine $La_2Mo_2O_9$ thin films on pre-heated alumina substrate using chemical spray pyrolysis method and studied its dielectric properties at high frequency region for microwave and fuel cell applications [45, 46].

2 Experimental

2.1 Synthesis of $La_2Mo_2O_9$ thin films

The spray pyrolysis route was employed to deposit LAMOX thin films onto pre-heated alumina (Al_2O_3) substrate. The following analytical grade chemicals were directly used for the synthesis of $La_2Mo_2O_9$ thin films without any further treatment. Lanthanum chloride ($LaCl_3.7H_2O$) and Molybdic acid (MoO_3H_2O) were used as a precursor with a proper molar concentration ratio for the synthesis of LAMOX thin film. The solubility of the lanthanum chloride and molybdic acid salts were found to be 957.00 g/L and 1.51 g/L in water at room temperature (25 °C). Due to this major differnce in the solubility factor, the

solutions of the lanthanum chloride and molybdic acid precursors were separately prepared. The specific amount of lanthanum chloride was dissolved in 15 ml of double-distilled water. On the other hand, molybdic acid was initially dissolved with a specific amount of concentrated HNO_3 under vigorous stirring for 15 min. at room temperature, and a further 15 ml of distilled water was poured drop wise to get a clear and transparent solution. The aqueous solution of lanthanum chloride was slowly added to an aqueous solution of molybdic acid and mixed thoroughly using magnetic stirring for 15 min. The resulting 30 ml aqueous solution mixture was transferred to the spray pyrolysis unit for LAMOX thin film synthesis. The synthesized LAMOX thin films were annealed at 1000 °C for two hours in an air atmosphere.

2.2 Characterization techniques of $La_2Mo_2O_9$ thin films

The crystal structure of LAMOX thin films was determined by a mini-flex X-ray diffractometer with Cu-Kα radiation (λ = 1.54 Å). The morphological study of LAMOX thin films was done using field emission scanning electron microscopy (FESEM, JEOL JSM-6500F). EDAX (Energy-dispersive X-ray spectroscopy) Oxford instruments model ASTM E1508-98 was used to determine the elemental composition with atomic and weight percent of deposited LAMOX thin films. Fourier transform infrared spectroscopy analysis of LAMOX thin films was carried out by FTIR (model Lambda-7600) in the range from 400 to 4000 cm^{-1}. The surface element analysis study of LAMOX was studied by using X-ray photoelectron spectrometer (XPS, thermos-scientific Inc. K-alpha) with a micro focus monochromatic Al-Kα X-ray source. The dielectric parameters of LAMOX material were directly measured using the LCR Q-meter (APLAB model 4300R) in the frequency range from 20 Hz to 300 kHz. The dielectric constant and dielectric loss of LAMOX material was also determined at different characterizing temperatures.

3 Results and discussion

3.1 Thermo-gravimetric and differential thermal analysis (TG—DTA) of LAMOX

The decomposition of crystalline lanthanum molybdenum oxide powder takes place from room temperature to 1000 °C, with heating and cooling rates of 10 °C min^{-1}, as shown in Fig. 1. TGDTA plot provides information about phase forming temperature of a material. Weight loss of the sample was made in two main steps about 652 °C [47, 48]. A total of 29.50% of weight loss occurs from room temperature to near about 550 °C [49], which corresponds to residual water elimination and decomposition of chlorine. In the second step, 2.34% weight loss occurs upto 650 °C, which refers to the decomposition and formation of the pure crystallization phase of $La_2M_2O_9$. DTA shows a strong endothermic peak at 546 °C, which corresponds to the crystallization of $La_2M_2O_9$. Above the 650 °C, no further weight loss was observed, which indicates the formation of stable crystalline phase. The R. A. Rocha, E. N. S. Muccillo were reported the phase formation of LAMOX at 550 °C [50].

3.2 XRD analysis

The crystallographic properties of annealed $La_2Mo_2O_9$ thin films were analysed by X-ray diffraction measurements, as shown in Fig. 2a–c. The Rietveld refinement of XRD patterns was carried out for 0.1 M, 0.15 M, and 0.2 M annealed powders at 1000 °C for

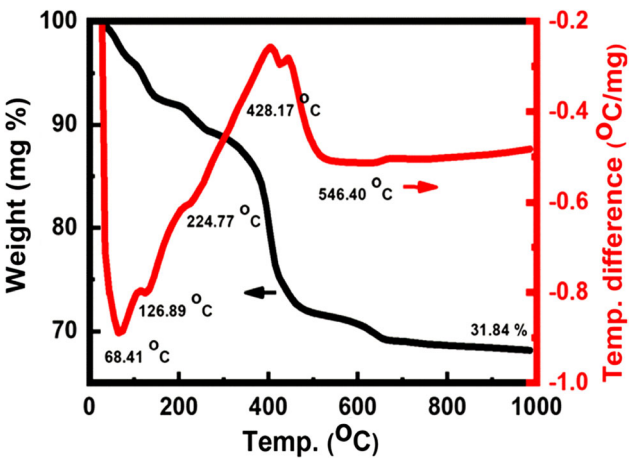

Fig. 1 TGDTA plot of synthesized LAMOX thin film

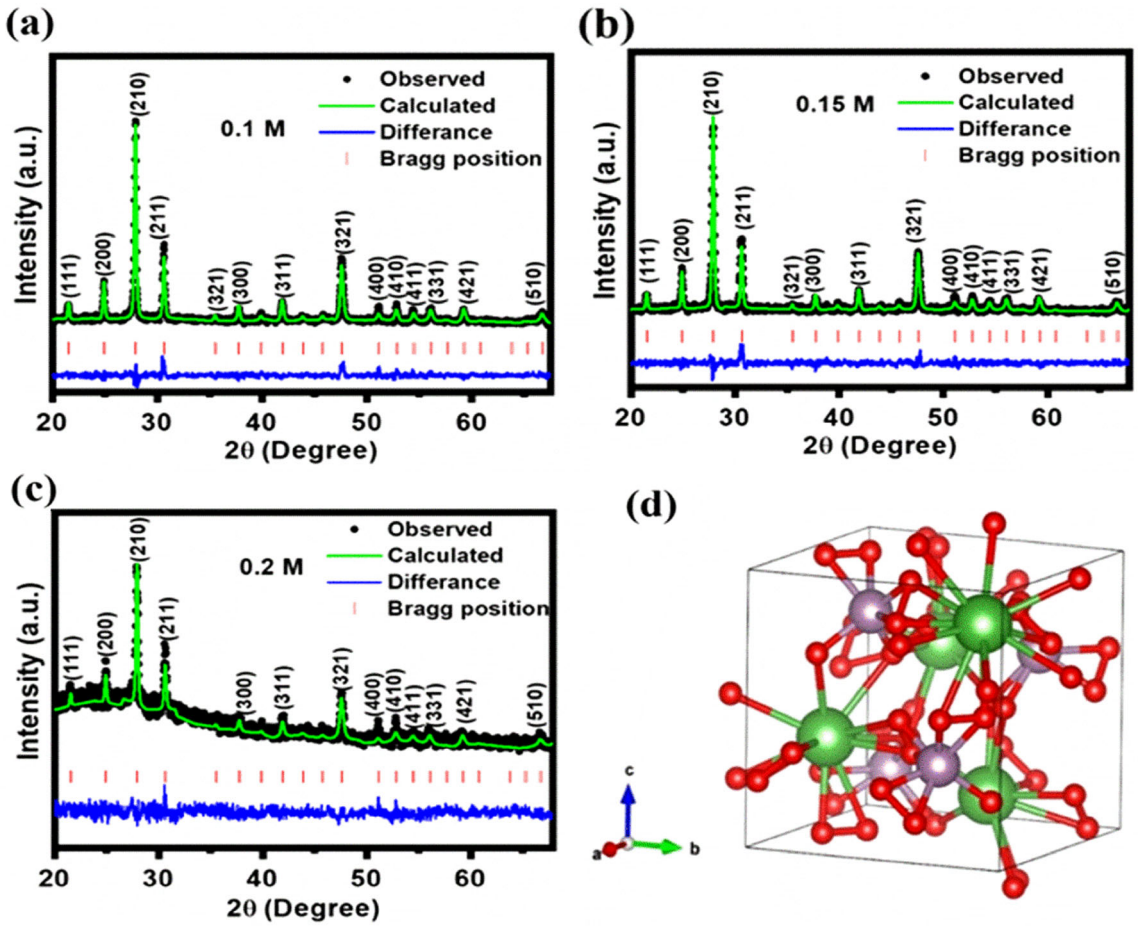

Fig. 2 Rietveld-refined XRD pattern. **a**–**c** Reitveld refinement patterns of the annealed $La_2Mo_2O_9$ with the different concentrations of 0.1 M, 0.15 M and 0.2 M. **d** Crystal structure of $La_2Mo_2O_9$

two hours. The refinement anlysis of LAMOX XRD patterns clearly confirm the formation of pure phase of cubic crystal strcture with $P2_13$ space group (Space group number 198) [51]. The diffraction pattern also well match with JCPDS card number 28-0509 of the $La_2Mo_2O_9$ cubic crystal structure [52]. Rietveld refinement was used to calculate lattice parameters using the Full-Prof suite software. The variation in derived lattice parameters can be seen in Table 1. The good agreement has been observed between previously reported and observed lattice parameters of $La_2Mo_2O_9$ [53]. It is observed that from concentration 0.1–0.2 M, the lattice parameters slightly increase with unit cell volume. The schematic unit cell crystal structure derived from output refinement data is shown in Fig. 2d. For crystal structure visualization purposes, the software package VESTA is used [54]. There is no literature study observed on the pure form of LAMOX phase. Siddharth, Sandip Bysakh, Anjan Sil have reported the refinement of W doped LAMOX for palletes where refinement data matches with JCPDS cared no. 28-0509 [55]

Table 1 Unit cell parameters for different concentrations of LAMOX films

Unit cell parameter	Concentration		
	0.1 M	0.15 M	0.2 M
χ^2	1.35	1.44	1.75
R_p	49.10	50.51	77.31
R_{wp}	32.90	33.80	66.90
R_{exp}	31.38	33.20	54.13
a = b = c (Å)	7.15	7.15	7.15
$\alpha = \beta = \gamma$	90°	90°	90°
ρ (gm/cm^3)	5.582	5.573	5.581
V (Å)^3	365.12	365.71	365.17

3.3 Surface morphology and elemental analysis

FESEM revealed morphological studies of deposited and annealed LAMOX thin films in air atmosphere. The effect of concentration on the morphology of deposited and annealed LAMOX thin films is revealed in Figs. 3, 4. The FESEM images of deposited 0.1 M LAMOX thin film is shown in Fig. 3a. In this case, the substrate wets more due to the partial evaporation of droplets during deposition. Furthermore, trapped solvent by material evaporated and left behind some porosity [56, 57]. Figure 4a shows the morphology of annealed 0.1 M $La_2Mo_2O_9$ thin film due to the complete evaporation of solvent developing cracks over the surface. This shows the minimizing of the surface energy and merging of grains into bigger grains [58]. The increase in concentration to 0.15 M, decreases the porosity of the thin film shown in Fig. 3b. However, after the annealing compact morphology was observed (Fig. 4b), the grain size increases after annealing up to 0.4 µm, and the grain size increases because minimizing the surface energy causes the merging of the grains to larger grains, for a higher concentration 0.2 M, (Fig. 3c), before wetting substrate vaporization of droplets takes place resulting in the formation of a lump of powder formed over substrate resulting in a highly porous and less adherent structure. The major cracks were observed because of solvent evaporation before reaching the substrate. After the annealing atom of material is aggregated and forms a lump which makes more cracks on the material (Fig. 4c), the annealing treatment increases the size of the lump of powder. Besides, the morphology also depends on the type of solution, solvent, substrate, and experimental setup.

Figure 5a–c shows the EDAX spectra of cubic LAMOX thin films after annealing at 1000 °C for two hours. Elemental composition obtained from EDAX of $La_2Mo_2O_9$ fairly well with the actual composition. The 1:1 atomic ratio of La and Mo was considered

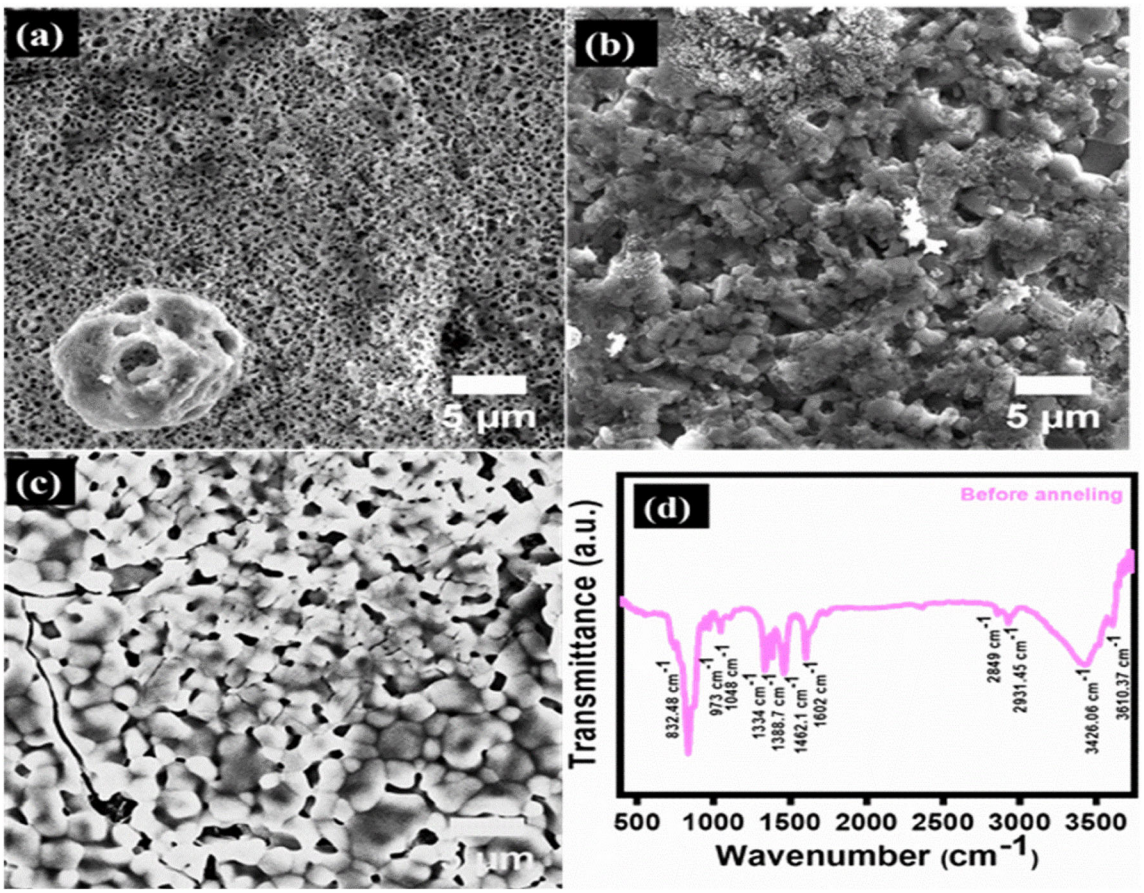

Fig. 3 **a**–**c** FESEM images of LAMOX film with 0.1 M, 0.15 M and 0.2 M, **d** FTIR spectra of LAMOX with 0.15 M

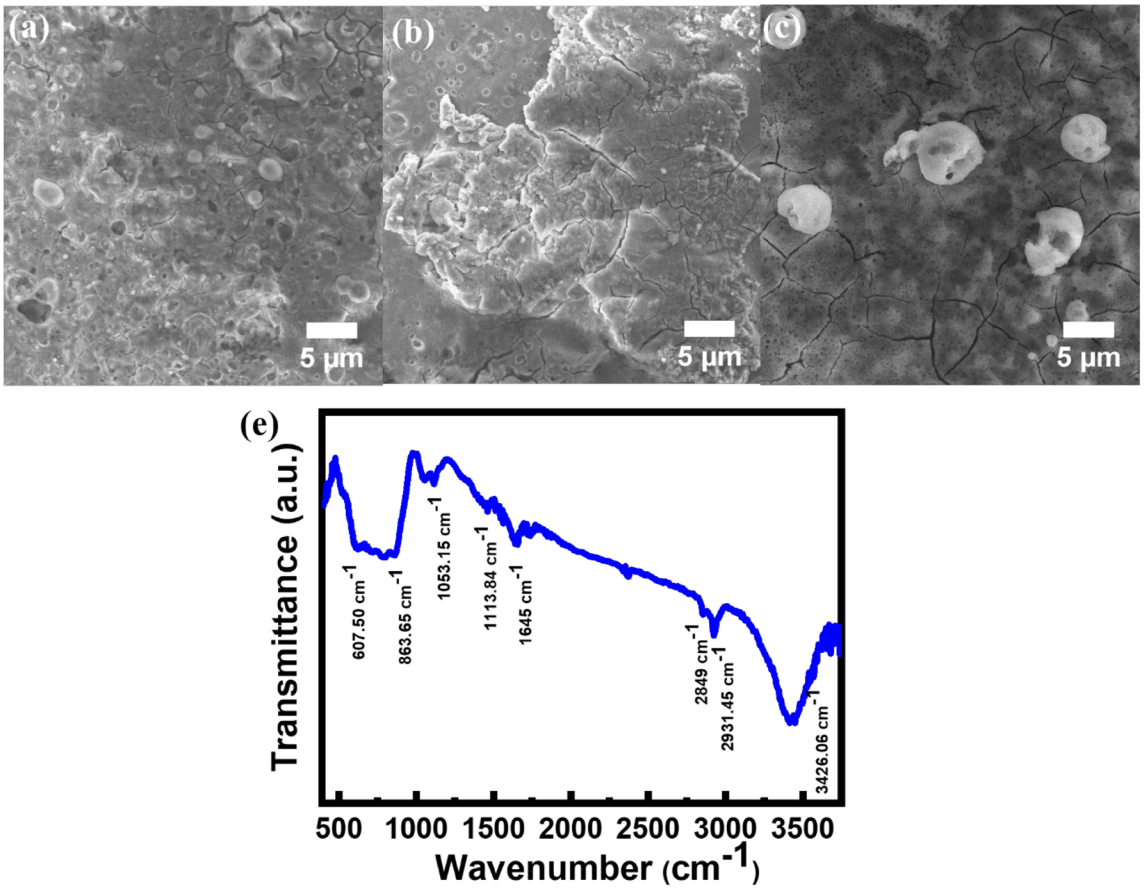

Fig. 4 **a**–**c** FESEM images of annealed $La_2Mo_2O_9$ with 0.1 M, 0.15 M and 0.2 M, **d** EDX mapping of 0.15 M annealed $La_2Mo_2O_9$, **e** FTIR spectrum of 0.15 M annealed $La_2Mo_2O_9$

during the synthesis of $La_2Mo_2O_9$ thin film. It shows the presence of only elements La, Mo, and O in LAMOX thin films. The EDAX analysis of annealed sample revealed the atomic ratio of La: Mo is 1:1.10.

3.4 Fourier transform infrared spectroscopy (FT-IR)

FTIR spectra are supportive of the characteristic appearance of La and Mo. The spectrum of LAMOX has been recorded from 400 to 4000 cm^{-1}. Figure 3d shows FT-IR spectra of LAMOX powder scratched from glass substrate deposited at 300 °C. The FTIR spectrum of deposited LAMOX at 300 °C shows the intense vibration band at 832.48 cm^{-1} due to stretching of La–O [50] and two consecutive vibrations observed at 972.47 and 1048.68 cm^{-1} are related to metal–oxygen bond arising from Mo–O [59]. The intermediate peaks at 1334, 1388.70 and 1462.10 cm^{-1} are consigned to the NO_2 stretching. The two small peaks at 2849 and 2931.45 cm^{-1} are assigned to N–H stretching. The vibration at 3426.06 and 3610.37 cm^{-1} are consigned to the water (H_2O) [60]. The FT-IR spectrum of LAMOX powder annealed at 1000 °C for two hours is shown in Fig. 4d. It shows the broad bands from 607.50 cm^{-1} to 863.65 cm^{-1} indicates the formation of metal oxide. The intensity of La–O and Mo–O bands is observed to decrease upon annealing due to the improved crystallization effect. The peaks at 3610.37 cm^{-1} disappear in the annealing spectra of FTIR because of the evaporation of water at high temperatures from the material.

3.5 X-ray photoelectron spectroscopy (XPS)

X-ray photoelectron spectroscopy (XPS) was used to determine the chemical composition and electronic structure of $La_2Mo_2O_9$ thin film.The XPS spectra for annealed 0.15 M $La_2Mo_2O_9$ films is shown in Fig. 6a–d. The XPS survey spectrum (Fig. 6a) demonstrates the presence of La, Mo and O elements. The high-resolution XPS spectrum of the La-3d core level is

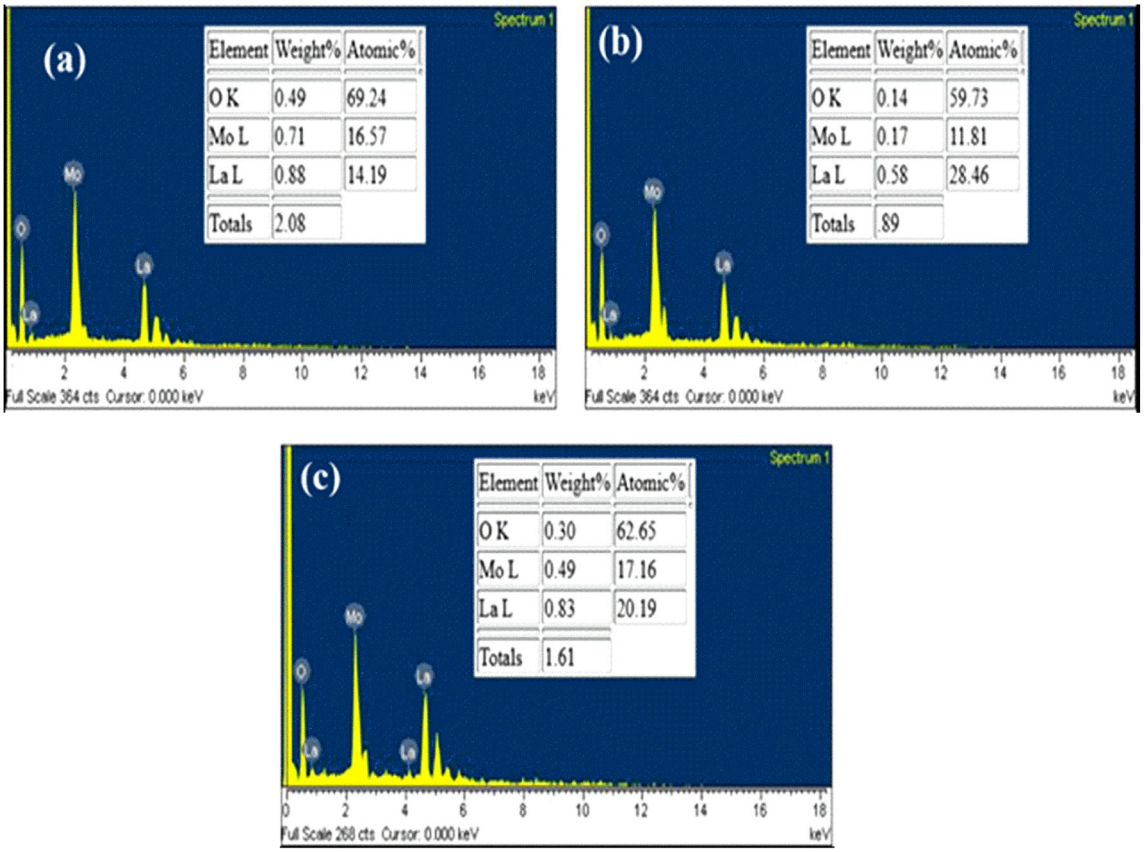

Fig. 5 EDX spectrum of annealed $La_2Mo_2O_9$. **a** 0.1 M, **b** 0.15 M, and **c** 0.2 M

decomposed into seven peaks, and this peak originates from the spin-orbital splitting of La $3d_{3/2}$ and La $3d_{5/2}$ states of $La_{(III)}$ [61, 62]. The high-resolution XPS spectrum of the Mo 3d core level at binding energy 232.20 and 235.31 eV corresponds to Mo^{+6} $3d_{5/2}$ and $3d_{3/2}$ [63–65]. The high-resolution O1s XPS spectrum shows (Fig. 6d) a central peak at 530 eV, which corresponds to oxygen ions inside the lattice, while the line at 531.21 eV corresponds to adsorbed oxygen [66].

3.6 Temperature dependent dielectric constant

Figure 7a–i shows variation in dielectric constant (ε′) for $La_2Mo_2O_9$ thin films as a function of temperature at different frequencies. Figure 7a–b indicates a directly proportional relation of ε′ with temperature, the abrupt growth in the ε′ describes the phase transition of $La_2Mo_2O_9$ [50]. The polarization property of $La_2Mo_2O_9$ shows the directly proportional relation between dielectrics constant and temperature. The dielectric constant (ε′) was calculated using the relation [67].

$$\varepsilon' = \frac{Ct}{\varepsilon_0 A} \tag{1}$$

where C is the capacitance in pF, t is the thickness of the sample in cm, A is Area of the cross-section, ε_0 is permittivity of free space and ε' is the dielectric constant.

The dielectric constant slowly increases in its initial stage due to its properties like high resistivity, presence of impurities and defects within the material and then it rapidly increases from specific temperature called as transition temperature of LAMOX, after attaining a maximum value it start to decreases. All the samples of $La_2Mo_2O_9$ show two relaxation peaks in the temperature range 700–750 °C. The shifting of peaks is observed toward the high-temperature side with rising frequency, and the height of the peaks decreases with increasing concentration of $La_2Mo_2O_9$. Multiple dielectric relaxation peaks shows several relaxation phenomena due to randomly distributed oxygen ions vacancies [68].

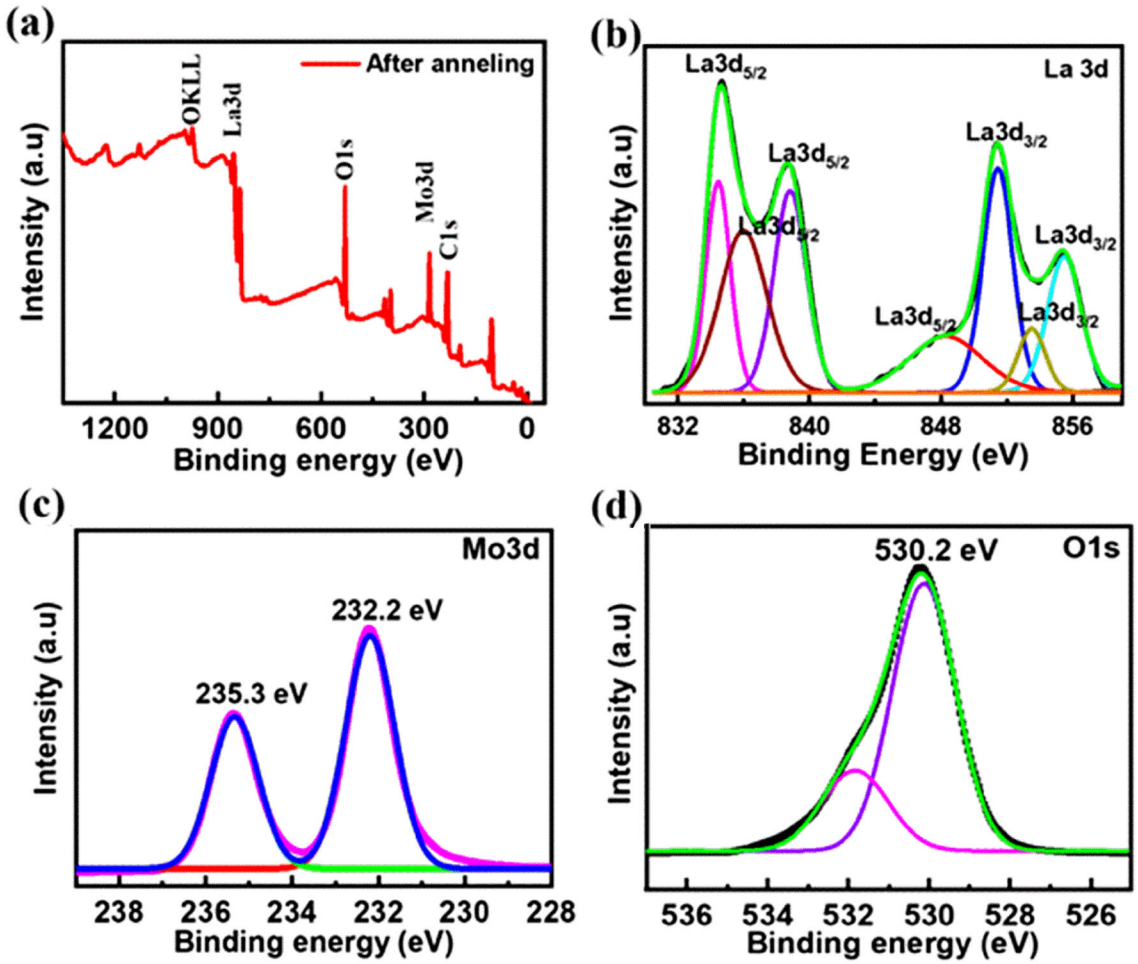

Fig. 6 Chemical analysis. **a** Survey of XPS spectrum, **b** XPS spectra of La 3d, Mo 3d and O 1s of 0.15 M annealed $La_2Mo_2O_9$

The variation of ε′ of $La_2Mo_2O_9$ with temperature is shown in Fig. 7a–i. The dielectric constant of $La_2Mo_2O_9$ shows fragile dependency on temperature up to 200 °C, indicating thermal stability of dielectric properties of $La_2Mo_2O_9$. The increase in dielectric constant with temperature at their initial state causes increase in internal stresses which influence the domain wall motion. The temperature dependency of domain wall motion has confirmed from increase of dielectric constant at critical temperature [69]. As concentration of LAMOX increases, a slightly increase in transition temperature is observed.

With distinct frequency dispersion, the significant increase in ε′ were observed, which means that at elevated temperatures, the frequency-dependent dielectric polarizability contributes to dielectric properties. The concentration of $La_2Mo_2O_9$ films systematically suppresses the height of the dielectric peak for 1, 10 and 100 kHz at 675 °C and 750 °C. Table 2 shows the variation in dielectric constant with frequency as a function of the concentration of LAMOX thin films.

3.7 Frequency-dependent dielectric constant

The dielectric properties of LAMOX thin films as a function of frequency is based on the interaction of external field with the electric dipole moment of the LAMOX material. Frequency-dependent variation of ε′of LAMOX at different annealing temperatures are shown in Fig. 8a–e and corresponding value of dielectric constant listed in Table 2. Figure indicates the inverse relation between the dielectric constant with applied frequency. During this variation, dielectric dispersion is observed at a lower frequency region and attains a constant value at higher frequency side, which confirms the behavior of the

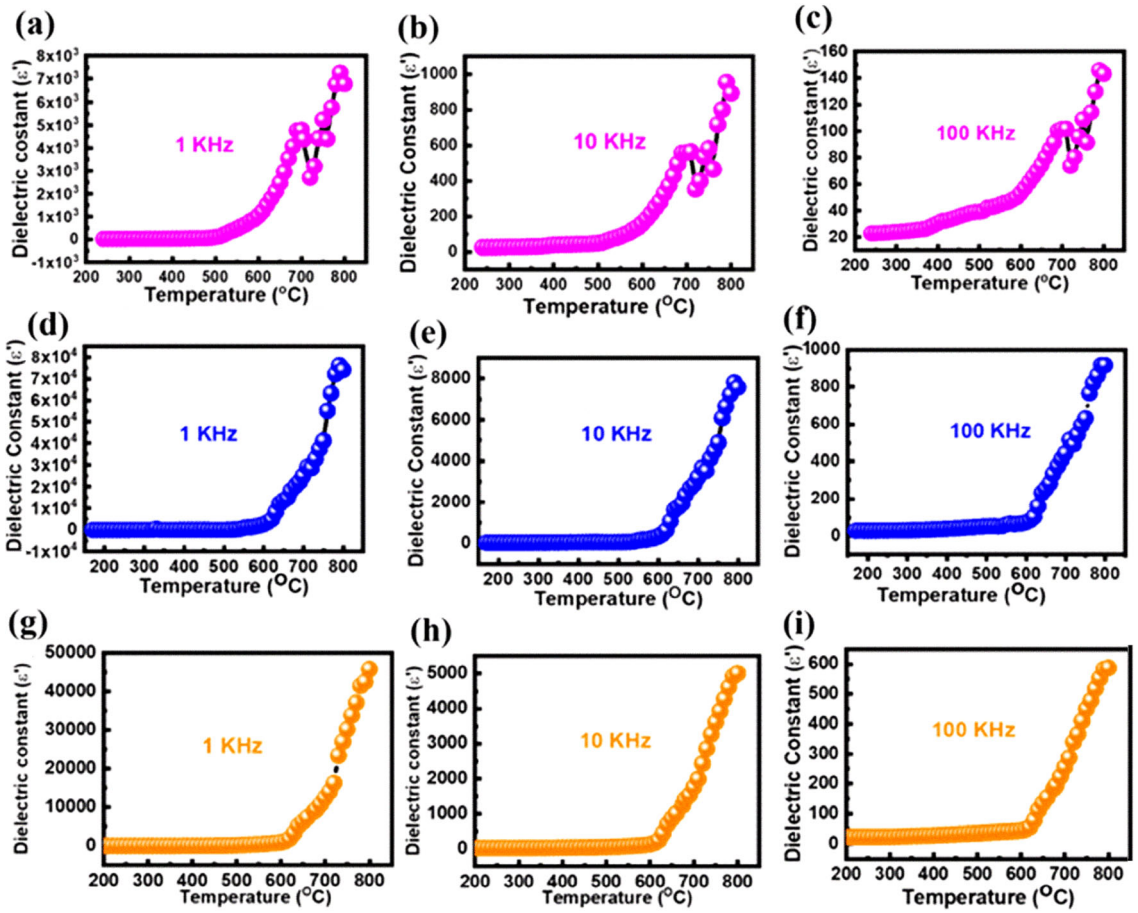

Fig. 7 **a**–**c** Dielectric constant Vs temperature of 0.1 M annealed $La_2Mo_2O_9$ at 1 kHz, 10 kHz and 100 kHz, **d**–**f** Dielectric constant Vs temperature of 0.15 M annealed $La_2Mo_2O_9$ at 1 kHz, 10 kHz and 100 kHz, **g**–**i** Dielectric constant Vs temperature of 0.2 M annealed $La_2Mo_2O_9$ at 1 kHz, 10 kHz and 100 kHz

Table 2 Variation in dielectric constant with frequency is a function of concentration of LAMOX thin films

Frequency (kHz)	Temperature (°C)	Concentration		
		0.1 M	0.15 M	0.2 M
1	Room temperature	38.32	26.78	50.03
10		37.50	21.86	34.96
100		37.05	19.95	30.89
1	100	25.35	31.37	28.95
10		24.80	30.88	27.93
100		24.57	30.65	27.63
1	200	25.45	32.66	30.15
10		24.42	31.51	29.01
100		24.19	31.30	28.69
1	300	35.96	38.36	38.54
10		29.28	33.94	32.18
100		26.44	32.24	30.01
1	400	57.90	44.86	49.37
10		41.42	39.62	39.79
100		31.29	34.49	32.59

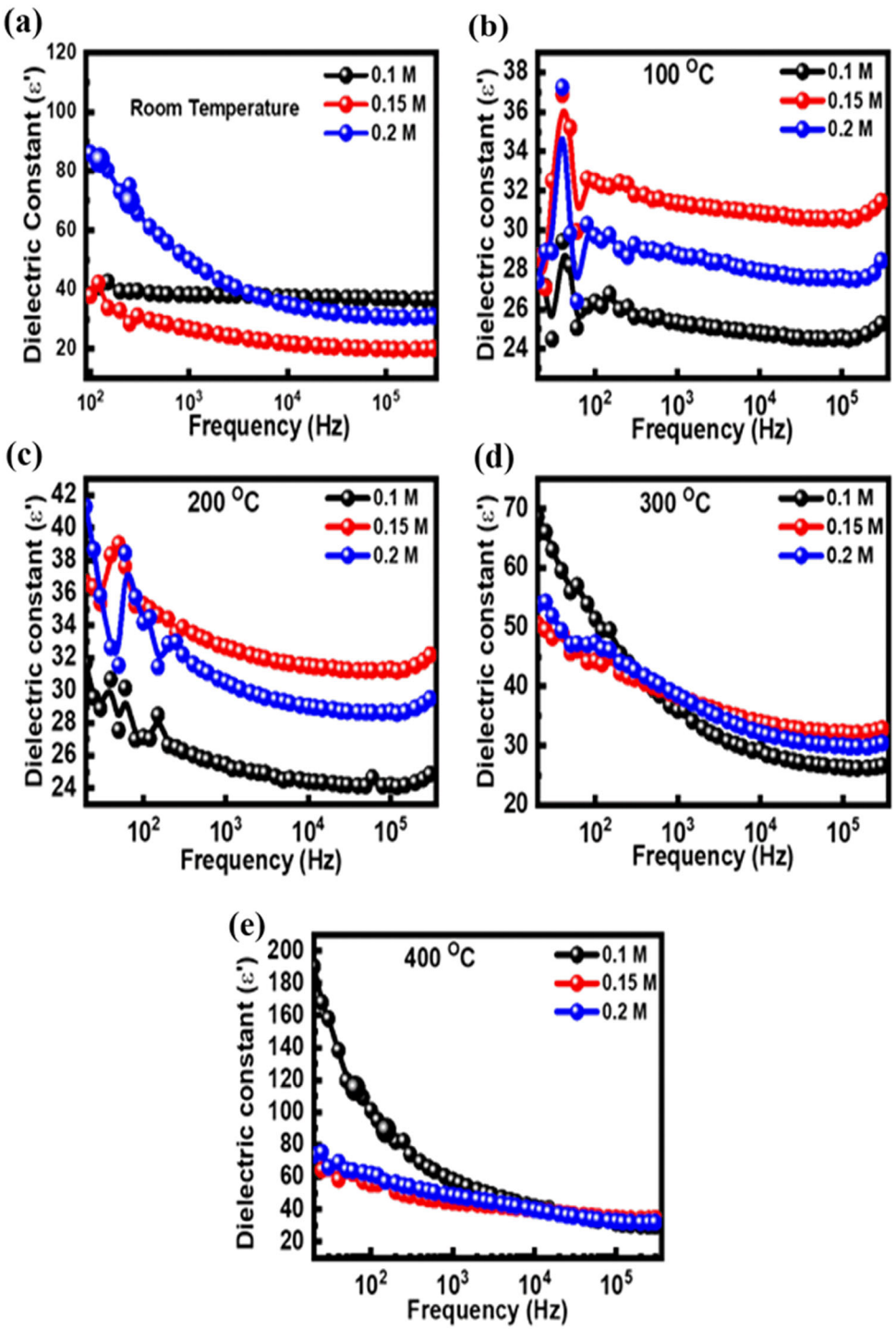

Fig. 8 Dielectric constant Vs frequency for annealed $La_2Mo_2O_9$ at **a** Room temperature, **b** 100, **c** 200, **d** 300, **e** 400 °C

normal dielectrics [70, 71]. Usually dielectric constant can influence by applied frequency due to the relaxation time of charge transport.

The samples exhibit dielectric dispersion because of Maxwell–Wagner inter-facial polarization, which depends on Koop's phenomenological theory [72]. According to this, the inhomogeneous dielectric is made up of well-conducting grains kept separated by low conducting grain boundaries [73]. Grain boundaries and grains are active at lower and higher frequencies respectively. Thus, at a lower frequency ε′ is maximum and at a higher frequency it minimum [74]. The dielectric dispersion is associated with very high polarization caused by charge migration

through limited paths and may be attributed to dipoles caused by changes in cation valence states and space charge polarization [75].

The dielectric constant (ε′) of LAMOX is subsidized by numerous structural and microstructural factors. These factors are inter-facial dislocations, oxygen vacancies, porosity, grains, grain boundaries, etc. [76]. The inhomogeneity in the present LAMOX structure was observed due to the vacancies and grain. Sometimes even electronic or ionic hopping mechanisms result in electronic polarization subsidizing the low-frequency dispersion. Because of the molecules inertia, the ionic and orientational polarizability decrease which eventually disappear at higher frequencies [77].

Thus, it is also observed that at a lower frequency site the ε′ possesses a higher value, thereafter decreases with applied frequency, and finally remains constant at a higher frequency. It could be endorsed to the influence of the multi-component polarizability [78, 79]. As frequency increases, dipoles will no longer be able to rotate sufficiently, causing their oscillations lag behind the external field. As a result, at high frequencies, the dielectric constant approaches a limited value [80]. The dielectric constant of $La_2Mo_2O_9$ films under investigation was found to be increases with characterizing temperature. This may be attributed to formation of nano-sized grains. This material exhibited dielectric dispersion at lower frequencies and a constant value at higher frequencies, which referred as its static value. For this sample, the static dielectric constant is close to 35. It is initiating that ε′ values increase with rising the temperature. This can be endorsed to the lower polarizability of La ion as compared to Mo ion. The dielectric value of LAMOX is high at higher frequency and increases with increasing oxide ions hopping through the material.

3.8 Temperature-dependent dielectric tangent loss

The dielectric relaxation, also known as tan loss (tan δ). It is a measurement of the dissipation of electrical energy during dipole reorientation due to an applied electric field. The square of the dipole shape factor is predicted by the theory of point defect relaxation, which is based on an idea of point defect, such as a vacancy, creates an elastic or electric dipole that relaxation strength is proportional to defect concentration [81]. Point defects in the $La_2Mo_2O_9$ system are mostly due to oxygen vacancies resulting from the dielectric phenomenon. The Fig. 9a–e shows the concentration effect on tan δ and the relaxation mechanism: (i) peak height (strength) of the dielectric relaxation curve is higher at 0.15 M compared to 0.1 & 0.2 M, (ii) all $La_2Mo_2O_9$ samples have two dielectric relaxation mechanisms. Because dielectric relaxation strength is proportional to defect concentration [82].

The presence of a single dielectric relaxation peak indicates the system has a reorientation of oxygen vacancies associated with a relaxation frequency. Ionic conductivity rises as oxygen vacancies in ceramic electrolytes are reoriented, resulting in oxide ion hopping via vacancies [83]. As shown in Fig. 9a–c, all $La_2Mo_2O_9$ samples have twice relaxation peaks in the temperature range from 350 to 550 °C with increasing frequency the relaxation peak shifts to the higher temperature side and this dielectric relaxation occurrence can be attributed to a thermally activated process.

Multiple relaxation phenomena are caused by randomly distributed oxygen vacancies that are indicated by the presence of multiple dielectric relaxation peaks. La and Mo cations alternate at 4a positions in the $La_2Mo_2O_9$ phase, which forming a lattice of parallelopiped that are slightly distorted. The oxygen O1 positions (4a sites) are filled, while the oxygen O2 and O3 positions (12b) are only partially filled [84]. As a result, oxygen vacancy defects form at O2 and O3 sites. Thus, the dielectric relaxation of oxygen vacancies from O2 and O3 sites can be linked to two dielectric relaxation peaks. The possibility of oxygen ions migrating from O1 to O2 is sufficient produces a relaxation peak due to higher concentration of oxygen vacancy in O2 and O3 sites. When an oscillating electric field is applied, the migration processes of oxygen ions produce two dielectric relaxation peaks [85]. Similar result reported by R. Nazz et. al. in 2020 [50]. Table 3 shows the variation in dielectric loss with frequency is a function of concentration of LAMOX thin films at constant temperatures.

3.9 Frequency-dependent dielectric tangent loss

The frequency-dependent variation of dielectric relaxation or tangent loss of LAMOX thin films

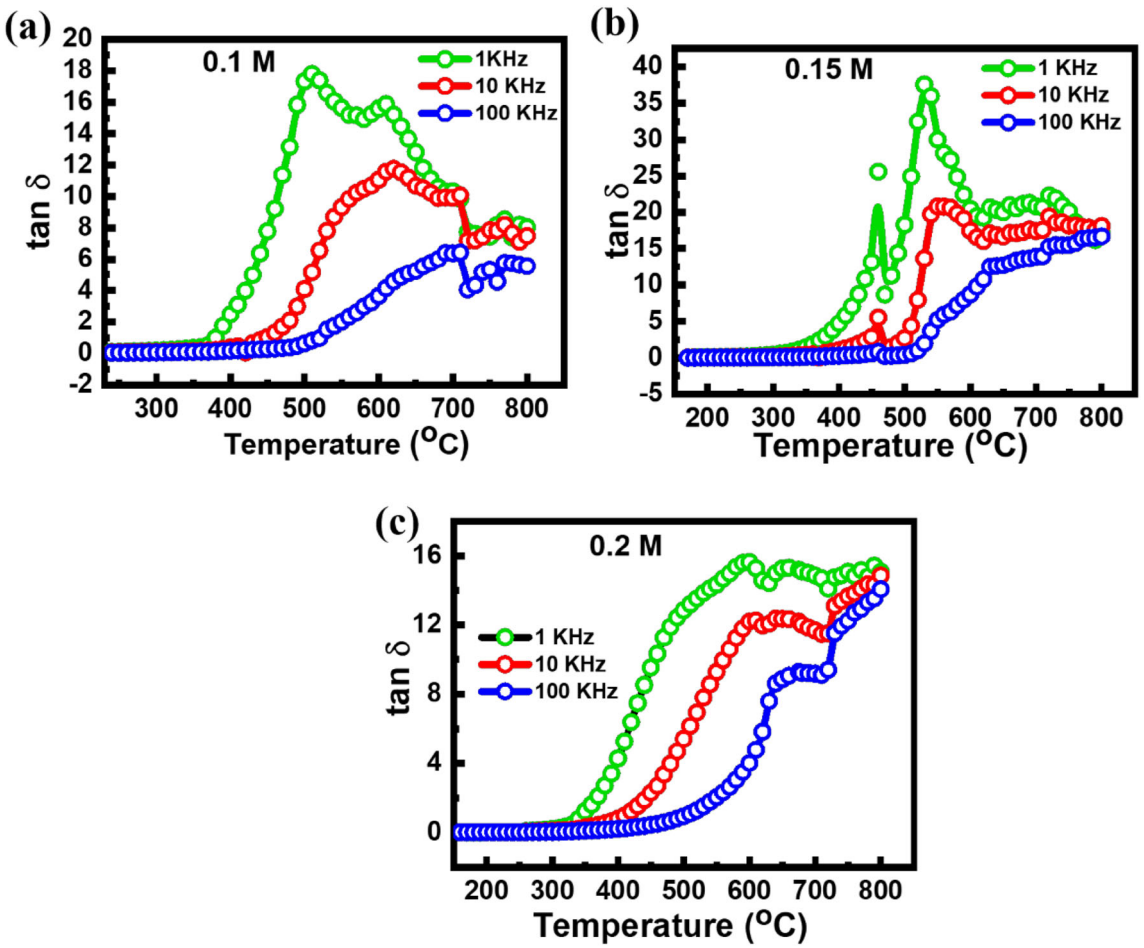

Fig. 9 **a** Dielectric loss Vs temperature of 0.1 M annealed $La_2Mo_2O_9$. **b** Dielectric loss Vs temperature of 0.15 M annealed $La_2Mo_2O_9$. **c** Dielectric loss Vs temperature of 0.2 M annealed $La_2Mo_2O_9$

Table 3 Variation in dielectric loss with frequency is a function of concentration of LAMOX thin films at constant temperatures

Frequency (kHz)	Temperature (°C)	Concentration		
		0.1 M	0.15 M	0.2 M
1	Room temperature	0.00	0.27	0.57
10		0.01	0.12	0.21
100		0.01	0.05	0.07
1	100	0.02	0.02	0.02
10		0.01	0.01	0.02
100		0.01	0.01	0.01
1	200	0.04	0.04	0.06
10		0.02	0.02	0.02
100		0.01	0.10	0.01
1	300	0.25	0.09	0.14
10		0.11	0.06	0.09
100		0.05	0.03	0.04
1	400	0.84	0.12	0.17
10		0.31	0.10	0.15
100		0.18	0.08	0.11

studied at different temperatures in frequency range from 20 Hz to 300 kHz is shown in Fig. 10a–e. The variation of dielectric loss with frequency for different concentration listed in Table 3. All the samples under investigation shows a decreasing tangent loss with frequency [86–89]. Domain wall resonance is thought to be the cause of this loss factor curve. At higher frequency site, the losses are low because of domain wall motion is inhibited. It also explained with collective behavior of p and n-type charge carriers are formed during sintering [90]. The p-type charge carriers experience local displacement in the opposite direction whereas n-type charge carriers reduces polarization at low frequencies [91].

The maximum dielectric loss is small when the relaxation time is large in comparison to the period

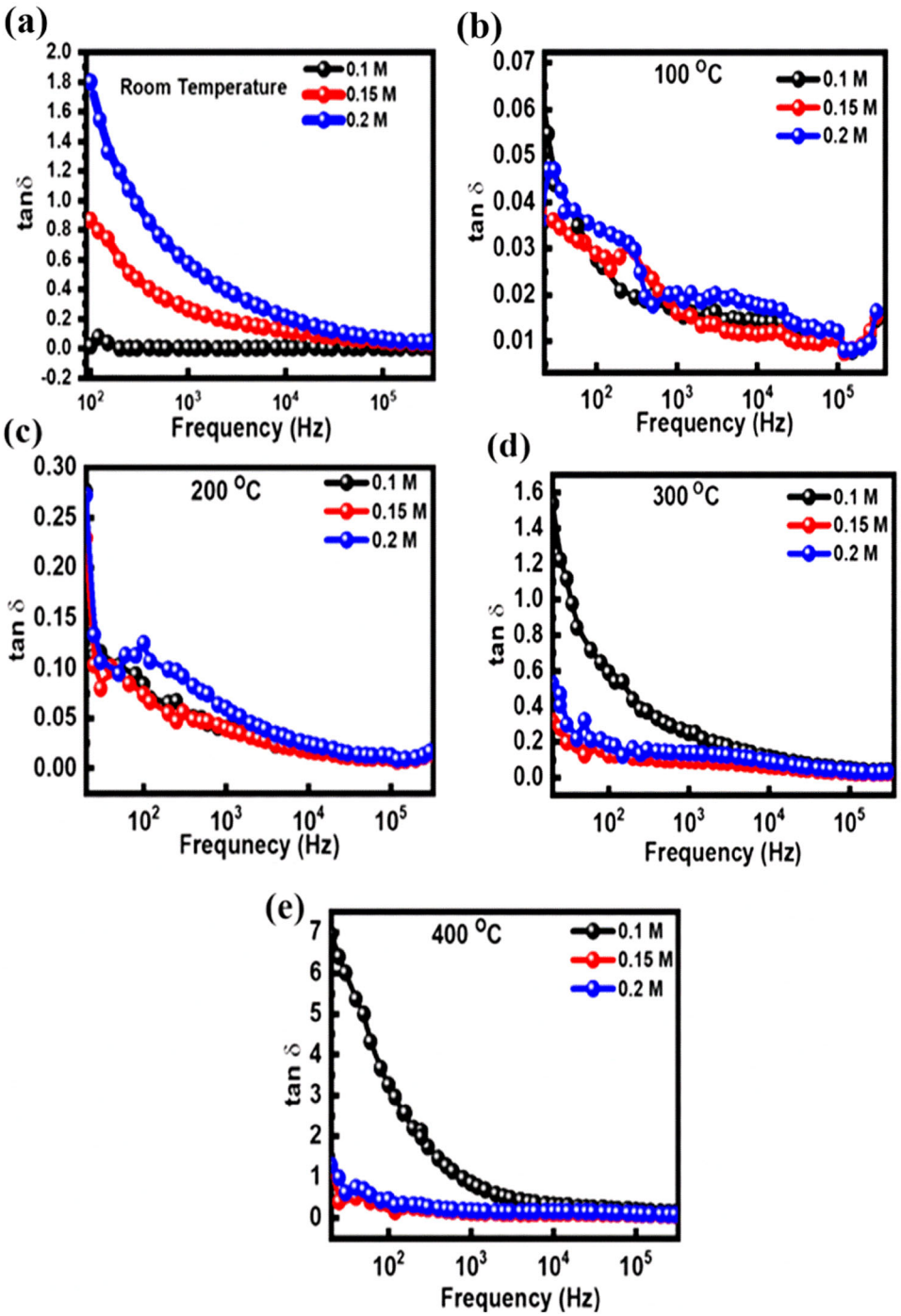

Fig. 10 Dielectric loss Vs frequency for annealed $La_2Mo_2O_9$ at **a** Room temperature, **b** 100, **c** 200, **d** 300, **e** 400 °C

and frequency of the applied field [92]. The dielectric loss remains almost constant beyond 100 kHz. This may be due to at greater frequency the domain wall motion is reserved and polarization is forced to alteration by rotation. It caused by the presence of vacancies and structural non-homogeneities. The decrease in tanδ at greater frequencies is in agreement with Koop's phenomenological model.

3.10 A.C conductivity

Figure 11a–c shows the temperature dependence AC conductivity (σ_{AC}) at different frequencies. The AC conductivity was calculated by using the following relation.

$\sigma_{AC} = 2\pi f \varepsilon_o \varepsilon' \tan\delta$[93]. Where, f is applied frequency, ε_o is permittivity of free space, ε' is dilectric constatnt and tanδ is the loss tangent. The conductivity model is represented by two distinct areas. First, the conductivity in the low-frequency range is frequency-independent, which characterizes the direct conductivity by displacement of charge carriers. Second, the dispersion regime compatible with AC conductivity occurs at a higher frequency. The AC conductivity explained by hopping model. The electron exchange between the ions in $La_2Mo_2O_9$ enhanced with polarization by enhancing the σ_{AC} in the mechanism of conduction [94]. Moreover, the σ_{AC} enhansed with rise in temperature due to the thermal energy's vibrations. The AC conductivity is very high for 0.2 M $La_2Mo_2O_9$.

3.11 DC conductivity

The behavior of DC conductivity of $La_2Mo_2O_9$ with temperature is shown in Fig. 11d. It shows semiconducting behavior, carrier concentration of carriers increases as temperature rises, resulting in an increase in conductivity. In the case of $La_2Mo_2O_9$, the mobility of the charge carrier are directly proportional to the temperature and no change in carrier

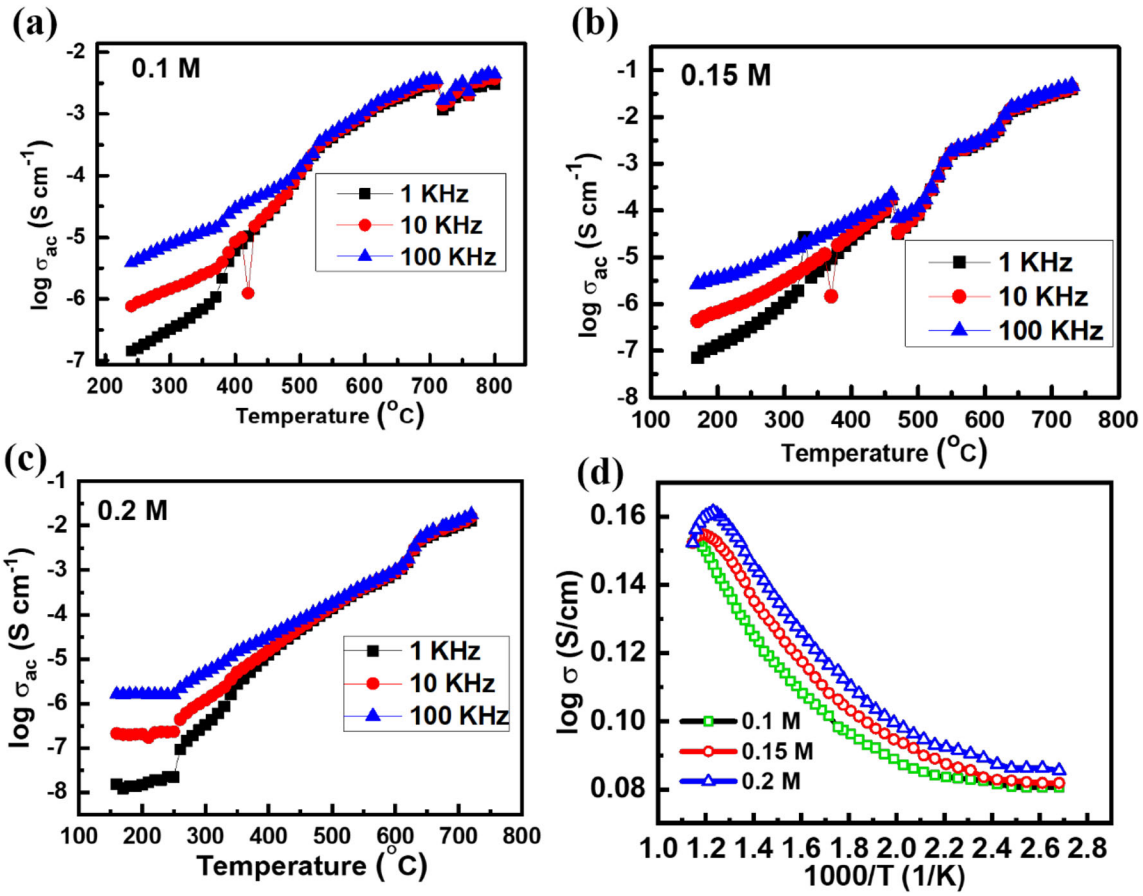

Fig. 11 **a–c** AC conductivity of annealed $La_2Mo_2O_9$ at various frequencies of 0.1 M, 0.15 M, and 0.2 M. **d** DC conductivity of annealed $La_2Mo_2O_9$ of 0.1 M, 0.15 M, and 0.2 M

concentration is observed. All of the $La_2Mo_2O_9$ samples shows the semiconducting behavior. Figure 11d shows DC conductivity (σ) of $La_2Mo_2O_9$. The heating rate of $La_2Mo_2O_9$ was approximate 1 K/min and scan the sample over the range of 353–873 K. Around the 823 K observed step-like variation, which shows the phase transition of $La_2Mo_2O_9$. The observed lower phase transition in $La_2Mo_2O_9$ crystalline sample is near about 823 K [95].

A break in the linearity nature of DC conductivity of $La_2Mo_2O_9$ is found near point 1.20 (560 °C). This break indicates the phase transition of $La_2Mo_2O_9$ from monoclinic to cubic phase. The breaking point of the linearity nature of DC conductivity of $La_2Mo_2O_9$ is called Curie temperature [96], and the value of DC conductivity at 600 °C is about 0.21, 0.17, and 0.23 μS/cm for 0.1 M, 0.15 M and 0.2 M $La_2Mo_2O_9$ respectively, this is much small value of DC conductivity than macrocrystalline sample (0.06 S/cm). Because highly disordered material near grain boundaries has lower conductivity than material within the grain, and submicron crystalline samples have many more regions of grain boundaries, this behavior can be inferred from their involvement.

3.12 Impedance of $La_2Mo_2O_9$

The complex impedance plot is obtained by plotting –Z″ versus Z′ . The impedance spectra of $La_2Mo_2O_9$ annealed thin films. The impedance studied at a temperature of 200 °C, 300 °C, and 400 °C for 0.1 M, 0.15 M, and 0.2 M of LAMOX thin films shows Cole–Cole plot. Figure 12a–i shows the observed impedance spectra for $La_2Mo_2O_9$. In the low-frequency region for temperatures of 200 °C, 300 °C, and 400 °C correspond to conduction due to grain boundary volume shown in Fig. 12a–i. This gives the grain boundary volume plays a major role in the conduction mechanism [97]. The grain boundary resistance is out of measurement scale in a low-frequency region, indicating some other relaxation phenomena that occur outside the measured frequency range. For 0.15 M $La_2Mo_2O_9$ at 500 and 600 °C, there are two semicircular arcs shown in Fig. 13a, b, one at the low-frequency cause of grain boundary conduction and another at the high-frequency range due to grain conduction [98]. Semicircle plots between the Z′ and –Z″ represent non-debye types of relaxation behavior. A non-debye relaxation is a dielectric component with multiple relaxation times denoted by τ [87]. It is nothing but the time required for the dipole to orient in the direction of the applied electric field. At lower frequency side, oxide ions and vacancies have more time to migrate through the electrode–electrolyte interface. As a result, the oxide ion vacancies that migrate across the interface are accumulate, resulting in the formation of the space charge barrier. This resistance appears as a linear curve on the lower frequency sides of the applied ac electric field. The shifting of impedance arc to the higher frequency range takes place as temperature increases, according to non-Debye relaxation phenomena [99]. This leads to the disappearance of impedance arc at higher temperatures due to grains [100]. The modulus formulation can explain the short and long-range hopping of the oxide ions through the vacant sites, as well as their jump probability. The imaginary part of modulus formalism explains the nature of oxide ion hopping as temperature changes. The grain boundary is critical to the overall electrical conductivity of the material. According to Baurele [101], the use of YSZ electrolyte impedance spectroscopy delivered a suitable technique for analyzing grain interior and grain boundary conductivities. According to this theory, the grain boundary acts as a barrier to oxide ion migration. The grain boundary blocking effect refers to the increased resistance to oxide ion movement provided by grain boundaries.

4 Conclusion

The dense and cores grain morphology was observed with some pores in LAMOX. FTIR spectra confirm the no surface impurities and assure pure phase formation of LAMOX. The elemental composition in films is affirmed with EDAX and is approximately equal to the precursor. The XPS results proved that Mo^{+6} cation is present in $La_2Mo_2O_9$ thin film. The dielectric constant studies shows multiple dielectric relaxation peaks with multiple relaxation phenomena due to randomly distributed oxygen ion vacancies. $La_2Mo_2O_9$ samples have twice the relaxation peaks in the temperature range 350—550 °C. With increasing frequency, the relaxation peak shifts to the higher temperature side; this dielectric relaxation occurrence can be attributed to a thermally activated process. When an oscillating electric field is applied, the migration processes of oxygen ions produce two dielectric relaxation peaks. The AC conductivity was

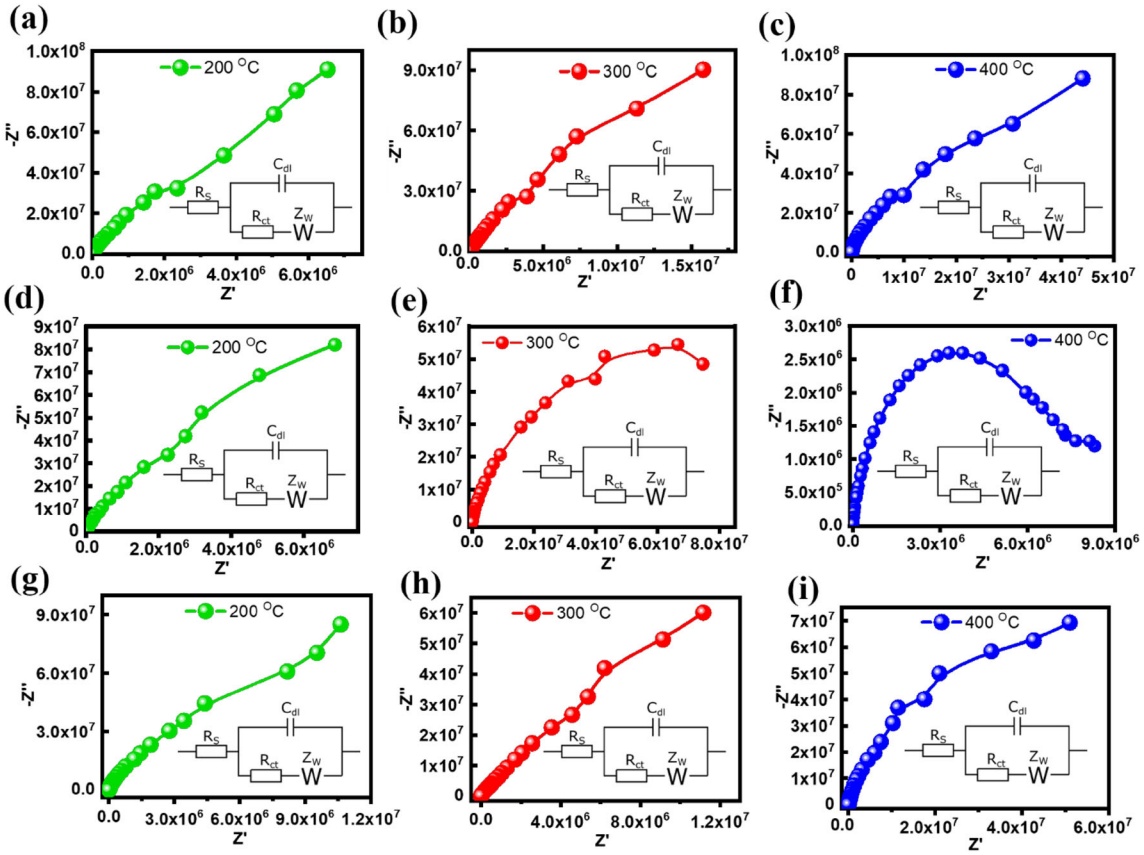

Fig. 12 **a** Impedance spectra of 0.1 M annealed $La_2Mo_2O_9$ at 200 °C, **b** Impedance spectra of 0.1 M annealed $La_2Mo_2O_9$ at 300 °C, **c** Impedance spectra of 0.1 M annealed $La_2Mo_2O_9$ at 400 °C, **d** Impedance spectra of 0.15 M annealed $La_2Mo_2O_9$ at 200 °C, **e** Impedance spectra of 0.15 M annealed $La_2Mo_2O_9$ at 300 °C, **f** Impedance spectra of 0.15 M annealed $La_2Mo_2O_9$ at 400 °C, **g** Impedance spectra of 0.2 M annealed $La_2Mo_2O_9$ at 200 °C, **h** Impedance spectra of 0.2 M annealed $La_2Mo_2O_9$ at 300 °C, **i** Impedance spectra of 0.2 M annealed $La_2Mo_2O_9$ at 400 °C

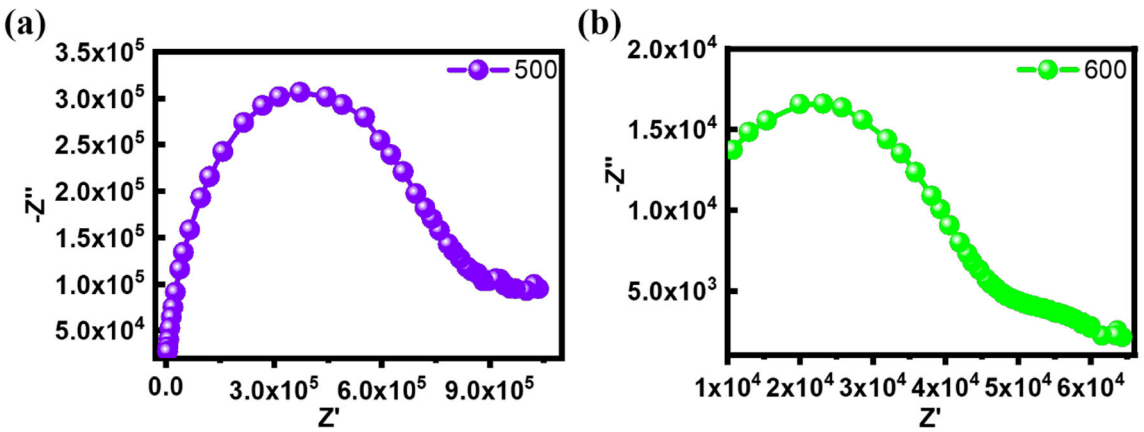

Fig. 13 **a** Impedance spectra of 0.15 M annealed $La_2Mo_2O_9$ at 500 °C, **b** Impedance spectra of 0.15 M annealed $La_2Mo_2O_9$ at 600 °C

explained by hopping model. The Arhenus nature is shown by the DC conductivity of $La_2Mo_2O_9$. The dielectric constant is high at lower frequency side due to high resistance of grain boundry and dielectric constant is low at higher frequency side due to grain conduction. Semicircle plots between the Z′ and – Z″ represent non-debye types of relaxation behavior of $La_2Mo_2O_9$.

Acknowledgements

This work was supported by department of physics National University Dong Hwa, Hualien, Taiwan.

Author contributions

All authors contributed to the study conception and design. Material preparation, data collection and analysis were performed by GAK, SAP and SAK. The first draft of the manuscript was written by GAK and SAK commented on previous versions of the manuscript. All authors read and approved the final manuscript.

Funding

The authors declare that no funds, grants or other support were received during the prepration of this mauscript.

Data availability

The data that support the findings of this study are available from the corresponding author Dr. R. K. Nimat on reasonable request.

Declarations

Conflict of interest Author have no financial or non financial interest to disclose.

References

1. X. Ren, Y. Wang, A. Liu, Z. Zhang, Q. Lv, B. Liu, Current progress and performance improvement of Pt/C catalysts for fuel cells. J. Mater. Chem. A **8**, 24284–24306 (2020)
2. I. Staffell, D. Scamman, A. Velazquez Abad, P. Balcombe, P.E. Dodds, P. Ekins, N. Shah, K.R. Ward, The role of hydrogen and fuel cells in the global energy system. Energy Environ. Sci. **12**, 463–491 (2019)
3. J. Liu, F. Yang, Z. Jiang, Y. Zhang, E. Hu, H. Wang, X. Yang, Enhanced ionic conductivity and durability of novel solid oxide fuel cells by constructing a heterojunction based on transition and rare earth metal co-doped Ceria. ACS Appl. Energy Mater. **4**, 13492–13503 (2021)
4. X. Li, X. Kuang, J. Sun, Rare earth elements based oxide ion conductors. Inorg. Chem. Front. **8**, 1374–1398 (2021)
5. M. Li, H. Niu, J. Druce, H. Téllez, T. Ishihara, J.A. Kilner, H. Gasparyan, M.J. Pitcher, W. Xu, J.F. Shin, L.M. Daniels, L.A.H. Jones, V.R. Dhanak, D. Hu, M. Zanella, J.B. Claridge, M.J. Rosseinsky, A CO_2-tolerant perovskite oxide with high oxide ion and electronic conductivity. Adv. Mater. **32**, 1905200 (2020)
6. W. Zhang, K. Fujii, T. Ishiyama, H. Kandabashi, M. Yashima, Dion–Jacobson-type oxide-ion conductor $CsLa_2Ti_2NbO_{10-\delta}$ without phase transitions. J Mater. Chem. A **8**, 25085–25093 (2020)
7. B. Santhoshkumar, K.R. Priolkar, S. Pollastri, D. Oliveira de Souza, I. Carlomagno, A.K. Bera, S.M. Yusuf, B. Pahari, Associating high oxide-ion conductivity and conduction mechanisms with local atomic environments in $Na_{0.5}Bi_{0.5-x}Ti_{1-y}MgyO_{3-\delta}$. J. Phys. Chem. C **125**, 19621–19630 (2021)
8. J.R. Peet, C.A. Fuller, B. Frick, M.M. Koza, M.R. Johnson, A. Piovano, I.R. Evans, Insight into design of improved oxide ion conductors: dynamics and conduction mechanisms in the $Bi_{0.913}V_{0.087}O_{1.587}$ solid electrolyte. J. Am. Chem. Soc. **141**, 9989–9997 (2019)
9. P. Lacorre, F. Goutenoire, O. Bohnke, R. Retoux, Y. Laligant, Designing fast oxide-ion conductors based on $La_2Mo_2O_9$. Nature **404**, 856–858 (2000)
10. F. Goutenoire, O. Isnard, R. Retoux, Crystal structure of $La_2Mo_2O_9$, a new fast oxide−ion conductor. Chem. Mater. **12**, 2575–2580 (2000)
11. W. Liu, W. Pan, J. Luo, A. Godfrey, G. Ou, H. Wu, W. Zhang, Suppressed phase transition and giant ionic conductivity in $La_2Mo_2O_9$ nanowires. Nat. Commun. **6**, 8354 (2015)
12. T.K. Paul, Y. Tsur, Influence of isovalent 'W' substitutions on the structure and electrical properties of $La_2Mo_2O_9$ electrolyte for intermediate-temperature solid oxide fuel cells. Ceramics **4**, 502–515 (2021)
13. F. Goutenoire, O. Isnard, E. Suard, O. Bohnke, Y. Laligant, R. Retoux, P. Lacorre, Structural and transport characteristics of the LAMOX family of fast oxide-ion conductors, based on lanthanum molybdenum oxide $La_2Mo_2O_9$. J. Mater. Chem. **11**, 119–124 (2001)
14. D.M. Zhang, Z. Zhuang, Y.X. Gao, X.P. Wang, Q.F. Fang, Electrical properties and microstructure of nanocrystalline $La_{2-x}A_xMo_2O_{9-\delta}$ (A = Ca, Sr, Ba, K) films. Solid State Ion. **181**, 1510–1515 (2010)
15. L. Malavasi, H. Kim, S.J.L. Billinge, T. Proffen, C. Tealdi, G. Flor, Nature of the monoclinic to cubic phase transition in the fast oxygen ion conductor $La_2Mo_2O_9$ (LAMOX). J. Am. Chem. Soc. **129**, 6903–6907 (2007)

16. L. Srijith, A. Das, H.P. Dasari, M.B. Saidutta, Electrical conductivity studies on LAMOX based electrolyte materials for solid oxide fuel cells. Ceram. Int. **48**, 29229–29237 (2022)
17. T. Paul, A. Ghosh, Correlation between structure and oxygen ion dynamics in Y substituted $La_2Mo_2O_9$ ionic conductors. AIP Adv. **6**, 095015 (2016)
18. B.B. Patil, A.D. Pawar, D.B. Bhosale, J.S. Ghodake, J.B. Thorat, T.J. Shinde, Effect of La^{3+} substitution on structural and magnetic parameters of Ni–Cu–Zn nano-ferrites. J. Nanostructure Chem. **9**, 119–128 (2019)
19. B.B. Patil, A.D. Pawar, S.S. Barate, J.S. Ghodake, J.B. Thorat, T.J. Shinde, Impact of La^{3+} substitution on electrical, magnetic, dielectric and optical properties of $Ni_{0.7}Cu_{0.1}Zn_{0.2}La_xFe_{2-x}O_4$ ($0 < x < 0.035$) system. J Rare Earths (2022). https://doi.org/10.1016/j.jre.2022.03.023
20. S.R. Yousefi, M. Masjedi-Arani, M.S. Morassaei, M. Salavati-Niasari, H. Moayedi, Hydrothermal synthesis of $DyMn_2O_5/Ba_3Mn_2O_8$ nanocomposite as a potential hydrogen storage material. Int. J. Hydrog. Energy **44**, 24005–24016 (2019)
21. R. Monsef, M. Salavati-Niasari, Architecturally robust tubular nano-clay grafted $Li_{0.9}Ni_{0.5}Co_{0.5}O_{2-x}/LiFeO_2$ nanocomposites: new implications for electrochemical hydrogen storage. Fuel **332**, 126015 (2023)
22. S.R. Yousefi, D. Ghanbari, M. Salavati-Niasari, M. Hassanpour, Photo-degradation of organic dyes: simple chemical synthesis of $Ni(OH)_2$ nanoparticles, $Ni/Ni(OH)_2$ and Ni/NiO magnetic nanocomposites. J. Mater. Sci. **27**, 1244–1253 (2016)
23. S.R. Yousefi, O. Amiri, M. Salavati-Niasari, Control sonochemical parameter to prepare pure $Zn_{0.35}Fe_{2.65}O_4$ nanostructures and study their photocatalytic activity. Ultrason. Sonochem. **58**, 104619 (2019)
24. S.R. Yousefi, A. Sobhani, H.A. Alshamsi, M. Salavati-Niasari, Green sonochemical synthesis of $BaDy_2NiO_5/Dy_2O_3$ and $BaDy_2NiO_5/NiO$ nanocomposites in the presence of core almond as a capping agent and their application as photocatalysts for the removal of organic dyes in water. RSC Adv. **11**, 11500–11512 (2021)
25. S.R. Yousefi, H.A. Alshamsi, O. Amiri, M. Salavati-Niasari, Synthesis, characterization and application of Co/Co_3O_4 nanocomposites as an effective photocatalyst for discoloration of organic dye contaminants in wastewater and antibacterial properties. J. Mol. Liq. **337**, 116405 (2021)
26. S.R. Yousefi, M. Ghanbari, O. Amiri, Z. Marzhoseyni, P. Mehdizadeh, M. Hajizadeh-Oghaz, M. Salavati-Niasari, $Dy_2BaCuO_5/Ba_4DyCu_3O_{9.09}$ S-scheme heterojunction nanocomposite with enhanced photocatalytic and antibacterial activities. J. Am. Ceram. Soc. **104**, 2952–2965 (2021)
27. M.A. Mahdi, S.R. Yousefi, L.S. Jasim, M. Salavati-Niasari, Green synthesis of $DyBa_2Fe_3O_{7.988}/DyFeO_3$ nanocomposites using almond extract with dual eco-friendly applications: photocatalytic and antibacterial activities. Int. J. Hydrog. Energy **47**, 14319–14330 (2022)
28. S.R. Yousefi, A. Sobhani, M. Salavati-Niasari, A new nanocomposite superionic system ($CdHgI_4/HgI_2$): synthesis, characterization and experimental investigation. Adv. Powder Technol. **28**, 1258–1262 (2017)
29. S.A. Kadam, G.T. Phan, D.V. Pham, R.A. Patil, C.-C. Lai, Y.-R. Chen, Y. Liou, Y.-R. Ma, Doping-free bandgap tunability in Fe_2O_3 nanostructured films. Nanoscale Adv. **3**, 5581–5588 (2021)
30. J.S. Rathore, L.V. Interrante, G. Dubois, Ultra low-k films derived from hyperbranched polycarbosilanes (HBPCS). Adv. Func. Mater. **18**, 4022–4028 (2008)
31. B. Sharma, R. Verma, C. Baur, J. Bykova, J.M. Mabry, D.W. Smith, Ultra low dielectric, self-cleansing and highly oleophobic POSS-PFCP aryl ether polymer composites. J. Mater. Chem. C **1**, 7222–7227 (2013)
32. Y. Liu, C. Qian, L. Qu, Y. Wu, Y. Zhang, X. Wu, B. Zou, W. Chen, Z. Chen, Z. Chi, S. Liu, X. Chen, J. Xu, A bulk dielectric polymer film with intrinsic ultralow dielectric constant and outstanding comprehensive properties. Chem. Mater. **27**, 6543–6549 (2015)
33. W. Volksen, R.D. Miller, G. Dubois, Low dielectric constant materials. Chem. Rev. **110**, 56–110 (2010)
34. Y. Huang, J. Economy, New high strength low-k spin-on thin films for IC application. Macromolecules **39**, 1850–1853 (2006)
35. G.-D. Fu, Z. Shang, L. Hong, E.-T. Kang, K.-G. Neoh, Nanoporous, ultralow-dielectric- constant fluoropolymer films from agglomerated and crosslinked hollow nanospheres of poly(pentafluorostyrene)-block-poly(divinylbenzene). Adv. Mater. **17**, 2622–2626 (2005)
36. X. Lei, M. Qiao, L. Tian, Y. Chen, Q. Zhang, Tunable permittivity in high-performance hyperbranched polyimide films by adjusting backbone rigidity. J. Phys. Chem. C **120**, 2548–2561 (2016)
37. H. Yamada, T. Shimizu, A. Kurokawa, K. Ishii, E. Suzuki, MOCVD of high-dielectric-constant lanthanum oxide thin films. J. Electrochem. Soc. **150**, G429 (2003)
38. P.G.A. Krishna, N.J. Tharayil, Dielectric properties of lanthanum oxide nanoparticle synthesized using chemical co-precipitation method. AIP Conf. Proc. **2162**, 020079 (2019)
39. V.Y. Ganvir, H.V. Ganvir, R.S. Gedam, Effect of lanthanum oxide addition on physical, electrical and dielectric

properties in lithium borosilicate glasses. Ferroelectrics **587**, 127–138 (2022)
40. M. Rajalakshmi, R. Indirajith, R. Gopalakrishnan, Single crystal growth of lanthanum(iii) molybdate(VI). J. Cryst. Process Technol. **04**, 7 (2014)
41. J.P. Fournier, J. Fournier, R. Kohlmuller, Bull. Soc. Chim. Fr **12**, 4277–4283 (1970)
42. P. Lacorre, R.J. Retoux, First direct synthesis by high energy ball milling of a new lanthanum molybdate. Solid State Chem. **132**, 443–446 (1997)
43. J. Zhang, L. Gao, Synthesis and characterization of nanocrystalline tin oxide by sol–gel method. J. Solid State Chem. **177**, 1425–1430 (2004)
44. D. Marrero-Lopez, J.C. Ruiz-Morales, P. Nunez, J.C.C. Abrantes, J.R. Frade, Synthesis and characterization of $La_2Mo_2O_9$ obtained from freeze-dried precursors. J. Solid State Chem. **177**, 2377–2386 (2004)
45. M. Raghasudha, D. Ravinder, P. Veerasomaiah, Influence of Cr_{3+} ion on the dielectric properties of nano crystalline Mg-Ferrites synthesized by citrate-gel method. Mater. Sci. Appl. **04**(07), 7 (2013)
46. L.B. Kong, S. Li, T.S. Zhang, J.W. Zhai, F.Y.C. Boey, J. Ma, Electrically tunable dielectric materials and strategies to improve their performances. Prog. Mater Sci. **55**, 840–893 (2010)
47. A.E. Gobichon, J.P. Auffrédic, D. Louër, Thermal decomposition of neutral and basic lanthanum nitrates studied with temperature-dependent powder diffraction and thermogravimetric analysis. Solid State Ionics **93**, 51–64 (1996)
48. B. Klingenberg, M.A. Vannice, Chem. Mater. **12**, 2575 (2000)
49. H. Sellemiab, S. Costea, A.B. Alib, R.R. Leila, S. Smirib, P. Lacorrea, Ceram. Int. **38**, 8853 (2013)
50. R.A. Rocha, E.N.S. Muccillo, Synthesis and thermal decomposition of a polymeric precursor of the $La_2Mo_2O_9$. Compd. Chem. Mater. **15**, 4268–4272 (2003)
51. R. Nazz, V. M. Gaikwad, V. Sathe, S. Anawane, S. A. Acharya, Correlation of dynamical disorder and oxy-ion diffusion mechanism in Dy, W co-doped $La_2Mo_2O_9$ system: electrolyte for IT-SOFCs. Dalton Trans. **49**, 13406–13419 (2020)
52. R.A. Rocha, E.N.S. Mucillo, Characterization of La_2MoO_6 prepared by the cation complexation technique. J. Alloy Compd. **400**, 83–87 (2005)
53. C. Tealdia, L. Malavasia, C. Ritterb, G. Flora, G. Costac, Lattice effects in cubic $La_2Mo_2O_9$: Effect of vacuum and correlation with transport properties. J. Solid State Chem. **181**, 603–610 (2008)
54. K. Momma, F. Izumi, VESTA 3 for three-dimensional visualization of crystal, volumetric and morphology data. J. Appl. Cryst. **44**, 1272–1276 (2011)
55. Siddharth, S. Bysakh, A. Sil, X-ray photoelectron spectroscopy and ion dynamics study of $W6^{+}$ doped $La_2Mo_2O_9$ as SOFC electrolyte. Mater. Res. Bullet. **105**, 36–44 (2018)
56. X. Zhu Fu, J. Li Luo, A.R. Sanger, N. Luo, K.T. Chuang, Y-doped BaCeO3−δ nano-powders as proton-conducting electrolyte materials for ethane fuel cells to co-generate ethylene and electricity. J. Power Sources **195**, 2659–2663 (2010)
57. J.X. Wang, X.P. Wang, F.J. Liang, Z.J. Cheng, Q.F. Fang, Enhancement of conductivity in $La_2Mo_2O_9$ ceramics fabricated by a novel three-stage thermal processing method. Solid State Ionics **177**, 1437–1442 (2006)
58. Z. Zhuang, X.P. Wang, A.H. Sun, Y. Li, Q.F. Fang, Sol–gel synthesis and transport property of nanocrystalline $La_2Mo_2O_9$ thin films. J. Sol-Gel. Sci. Technol. **48**, 315–321 (2008)
59. M. Guzik, M. Bieza, E. Tomaszewicz, Y. Guyotc, E. Zycha, G. Boulonc, Nd^{3+} dopant influence on the structural and spectroscopic properties of microcrystalline $La_2Mo_2O_9$ molybdate. Opt. Mater. **41**, 21–31 (2015)
60. R.A. Rocha, E.N.S. Muccillo, Particle size effect on formation and stability of β- $La_2Mo_2O_9$ ionic conductor. J. Alloy. Compd. **443**, 149–154 (2007)
61. L. Kövér, Z. Kovács, R. Sanjinés, G. Moretti, I. Cserny, G. Margaritondo, J. Pálinkás, H. Adachi, Electronic structure of tin oxides: high-resolution study of XPS and Auger spectra. Surf. Interface Anal. **23**, 461–466 (1995)
62. S. Hu, B. Chi, J. Pu, L. Jian, Novel heterojunction photocatalysts based on lanthanum titanate nanosheets and indium oxide nanoparticles with enhanced photocatalytic hydrogen production activity. J Mater Chem A **2**, 19260–19267 (2014)
63. C.J. Powell, Elemental binding energies for X-ray photoelectron spectroscopy. Appl. Surf. Sci. **89**, 141–149 (1995)
64. T.Y. Jin, M.V.M. Rao, C.L. Cheng, D.S. Tsai, M.H. Hung, Solid State Ionics **178**, 367 (2007)
65. T.L. Barr, S. Seal, K. Wozniak, J. Klinowski, J. Chem. Soc. Faraday Trans. **93**, 181 (1997)
66. G. Chen, B. Han, S. Deng, Y. Wang, Y. Wang, Y. Wang, Lanthanum dioxide carbonate $La_2O_2CO_3$ nanorods as a sensing material for chemoresistive CO_2 gas sensor. Electrochim. Acta **127**, 355–361 (2014)
67. A.V. Hippel, R.G. Breckenridge, F.G. Chesley, L. Tisza, High dielectric constant ceramics. Am. Chem. Soc. **38**, 1097 (1946)
68. J. Varghese, T. Siponkoski, M. Teirikangas, Structural, dielectric, and thermal properties of Pb free molybdate

based ultralow temperature glass. ACS Sustain. Chem. Eng. **4**, 3897–3904 (2016)
69. Z. Xing, C. Shen, C. Yin, H. Ye, C. Li, Low temperature synthesis and dielectric characterisation of $La_2Mo_2O_9$ ceramic at RF and microwave frequencies. Adv. Appl. Ceram. **119**, 387–392 (2020)
70. S. Saha, T.P. Sinha, Low-temperature scaling behavior of BaFe0.5Nb0.5O3. Phys. Rev. B **65**, 134103 (2007)
71. B. Behra, P. Nayak, R.N.P. Choudhary, Structural, dielectric and electrical properties of $NaBa_2X_5O_{15}$ (X = Nb and Ta) ceramics. Mater. Lett. **59**, 3489–3493 (2005)
72. B. Harihara Venkataraman, K.B.R. Varma, Frequency-dependent dielectric characteristics of ferroelectric $SrBi_2Nb_2O_9$ ceramics. Solid State Ionics **167**, 197–202 (2004)
73. G.A. Samara, Temperature and pressure dependences of the dielectric constants of semiconductors. Phys. Rev. B **27**, 3494 (1983)
74. C.G. Koops, On the dispersion of resistivity and dielectric constant of some semiconductors at audiofrequencies. Phys. Rev. **83**, 121 (1951)
75. Y. Zhi, A. Chen, Maxwell-Wagner polarization in ceramic composites $BaTiO_3$–$(Ni_{0.3}Zn_{0.7})Fe_{2.1}O_4$. J. Appl. Phys. **91**, 794 (2002)
76. S. Chougule, D. Patil, S.K. Chougule, Electrical conduction and magnetoelectric effect in ferroelectric rich (x)$Ni_{0.9}Zn_{0.1}Fe_2O_4$+(1–x) PZT ME composites. J. Alloys Compd. **452**, 205–209 (2008)
77. C.M. Kanamadi, L.B. Pujari, B.K. Chowgule, Dielectric behaviour and magnetoelectric effect in (x)$Ni_{0.8}Cu_{0.2}Fe_2O_4$+(1–x)$Ba_{0.9}Pb_{0.1}Ti_{0.9}Zr_{0.1}O_3$ ME composites. J. Magn. Mater. **295**, 139–144 (2005)
78. S.Y. Chu, C.H. Chen, Doping effects on the piezoelectric properties of low temperature sintered $PbTiO_3$-based ceramics for piezoelectric transformer applications. J. Mater. Sci. Lett. **20**, 615–617 (2001)
79. A. Srivastava, N. Mehta, Investigation of some thermos-mechanical and dielectric properties in multi-component chalcogenide glasses of Se–Te–Sn–Ag quaternary system. J. Alloy. Compd. **658**, 533–542 (2016)
80. N.A. Hegab, M. Fadel, I.S. Yahia, A.M. Salem, A.S. Farid, Electrical conductivity and dielectric properties of Se85Te15−x Sbx (x = 0 at.%, 2 at.%, 4 at.%, and 6 at.%) thin films. J. Electron. Mater. **42**, 3397 (2013)
81. A.S. Nowick, B.S. Berry, Anelastic relaxation in crystalline solids. Academic, New York **11**, 677 (1973)
82. F.P. Wang, Q.F. Fang, Mechanical and dielectric relaxation studies on the mechanism of oxygen ion diffusion in $La_2Mo_2O_9$. Phys. Rev. **65**, 064304–064306 (2002)
83. C. Ang, Yu. Zhi, L.E. Cross, Oxygen-vacancy-related low-frequency dielectric relaxation and electrical conduction in Bi:SrTiO3. Phys. Rev. B **62**, 228–234 (2000)
84. M. Weller, H. Schubert, Internal Friction, Dielectric Loss, and Ionic Conductivity of Tetragonal ZrO_2@3% Y_2O_3 (Y@TZP). J. Am. Ceram. Soc. **69**, 573–577 (1986)
85. D. Li, X.P. Wang, Q.F. Fang, J.X. Wang, C. Li, Z. Zhuang, Phase transition associated with the variation of oxygen vacancy/ion distribution in the oxide-ion conductor $La_2Mo_{2-x}WxO_9$, phys. Stat. sol. (a) **204**(7), 2270–2278 (2007)
86. S.R. Sinha, S.N. Choudhary, R.N.P. Chondhary, Phase transition in $Pb(Mg_{1/4}Cd_{1/4}W_{1/2})O3$ ceramics. J. Mat. Sci. Lett. **22**, 21–24 (2003)
87. G.G. Zhang, Q.F. Fang, X.P. Wang, Z.G. Yi, AC impedance and dielectric relaxation study on the effectsof the excess Pb introduced in $La_2Mo_2O_9$ oxide-ion conductors. Phys. Stat. Sol. (a) **199**, 329–334 (2003)
88. S.K. Sinha, R.N.P. Choudhary, S.N. Choudhary, T.P. Sinha, Structural and electrical behavior of $Pb(Mg_{1/4}Cd_{1/4}Mo_{1/2})O_3$ ceramics. J. Phys. Chem. Solids **63**, 323–329 (2002)
89. H.R. Rukmini, R.N.P. Choudhary, V.V. Rao, Structural and dielectric properties of Pb0.91(La, K)0.09(Zr0.65Ti0.35)0.9775O3 ceramics. J. Mat. Sci. **34**, 4815–4819 (1999)
90. S.R. Kulkarni, C.M. Kanmadi, B.K. Chowgule, Magnetic and dielectric properties of $Ni_{0.8}Co_{0.1}Cu_{0.1}Fe_2O_4$+PZT composites. J. Phys. Chem. Solids **67**, 1607–1611 (2006)
91. K.K. Patankar, V.L. Mathe, K.P. Mahajan, S.A. Patil, R.M. Reddy, K.V. Sivakumar, Dielectric behaviour and magnetoelectric effect in $CuFe_2O_4$–$Ba_{0.8}Pb_{0.2}TiO_3$ composites. Mat. Chem. Phys **72**, 23–29 (2001)
92. T. Paul, A. Ghosh, Ionic conductivity and dielectric relaxation in Y doped $La_2Mo_2O_9$ oxide-ion conductors. J. Appl. Phys. **116**, 144102 (2014)
93. K.M. Srinivasamurthy, K. Manjunatha, E.I. Sitalo, S.P. Kubrin, I.C. Sathish, S. Matteppanavar, B. Rudraswamy, V. Jagadeesha Angadi, Effect of Ce3+ substitution on the structural, morphological, dielectric, and impedance spectroscopic studies of Co–Ni ferrites for automotive applications. Indian J. Phys. **94**, 593–604 (2020)
94. K. Manjunatha, V.J. Angadi, M.C. Oliveira, S.R. de Lazaro, E. Longo, R.A.P. Ribeiro, S.O. Manjunatha, N.H. Ayachit, Towards shape-oriented Bi-doped $CoCr_2O_4$ nanoparticles from theoretical and experimental perspectives: structural, morphological, optical, electrical and magnetic properties. J. Mater. Chem. C **9**, 6452–6469 (2021)
95. K. Ishi, Kawa, Size effect on the ferroelectric phase transition in $PbTiO_3$ ultrafine particles. Phys. Rev. B **37**, 5852 (1988)

96. Z.G. Yi, Q.F. Fang, X.P. Wang, G.G. Zhang, Dielectric relaxation studies on the submicron crystalline $La_2Mo_2O_9$ oxide-ion conductors. Solid State Ionics **160**, 117–124 (2003)
97. S. Basu, H.S. Maiti, Ion dynamics in Ba-, Sr-, and Ca-doped $La_2Mo_2O_9$ from analysis of ac impedance. J. Solid State Electrochem. **14**, 1021–1025 (2010)
98. A. Kežionisa, D. Petrulionisa, E. Kazakevičiusa, S. Kazlauskasa, A. Žalgab, R. Juškėnas, Charge carrier relaxation phenomena and phase transition in $La_2Mo_2O_9$ ceramics investigated by broadband impedance spectroscopy. Electrochim. Acta **213**, 306–313 (2016)
99. S. Georgesa, O. Bohnkéa, F. Goutenoirea, Y. Laliganta, J. Fouletierb, P. Lacorrea, Effects of tungsten substitution on the transport properties and mechanism of fast oxide-ion conduction in $La_2Mo_2O_9$. Solid State Ionics **177**, 1715–1720 (2006)
100. A. Arulraj, F. Goutenoire, M. Tabellout, O. Bohnke, P. Lacorre, Synthesis and characterization of the anionic conductor system $La_2Mo_2O_{9-0.5x}F_x$ (x = 0.02−0.30). Chem. Mater. **14**, 2492–2498 (2002)
101. J. Liua, S. Hullb, I. Ahmed, S.J. Skinnera, Application of combined neutron diffraction and impedance spectroscopy for in-situ structure and conductivity studies of $La_2Mo_2O_9$. Nucl. Instrum. Methods Phys. Res., Sect. B **269**, 539–543 (2011)